Nanoscale

PAPER

View Article Online
View Journal | View Issue

Open Access Article. Published on 02 January 2026. Downloaded on 3/3/2026 10:50:38 PM.
This article is licensed under a Creative Commons Attribution-NonCommercial 3.0 Unported Licence.

Check for updates

Cite this: *Nanoscale*, 2026, **18**, 2264

Local deformations quantified with the common sublattice method

János L. Lábár, *[a] Ildikó Cora,[a] Béla Pécz,[a] Alexander Azarov [b] and Andrej Kuznetsov[b]

Received 17th September 2025,
Accepted 4th December 2025

DOI: 10.1039/d5nr03934g

rsc.li/nanoscale

Measurement of strain in epitaxial layers frequently faces the problem of localizing "perfectly" unstrained regions to use as a reference for the whole structure. Here, we develop a method for deducing such references in the unstrained substrate (with one crystal structure) to determine the local lattice deformations in the layer (with another crystal structure). The method works if there is a common sublattice in the layer and the substrate, so that the deviations from it may be used to interrelate the experimentally recorded data. The proof-of-concept is obtained using samples of cubic γ-Ga_2O_3 layers on a monoclinic β-Ga_2O_3 substrate, confirming that the new method overcomes several limitations of HRTEM-based methods. The precision of the method is ~0.5% in strain values.

Introduction

The importance of strain measurements is well known,[1] and the methods for strain measurement are reviewed in the literature, *e.g.*, by Gammer *et al.*[2] Elastic strain is related to lattice distortions and can be measured either starting from high-resolution transmission electron microscopy (HRTEM) images or from diffraction patterns (formed by either neutrons, X-rays or electrons). When large volumes are sampled (as in neutron or X-ray diffraction), one gets global lattice distortions, while electron-microscopy-based methods provide local information from nanosized volumes. The HRTEM-based peak pairs algorithm (PPA) locates the positions of atomic columns in real space.[3] Chen *et al.* extended the usage of PPA to crystals with low symmetries.[4] Ophus made an extensive comparison of 4D-STEM methods with many applications, such as the measurement of strain among them.[5] HRTEM-based geometrical phase analysis (GPA) of strain[6] starts with a real-space image, Fourier transformed into a reciprocal-space pattern, equivalent to a diffraction pattern, so that it can also be treated together with the other "diffraction" methods. Feng used GPA to determine strain in 2D crystals.[7] Wang *et al.*[8] and Lábár *et al.*[1] applied lattice fitting to improve the accuracy of the measurement of positions of diffraction disks and spots, respectively, in 4D-STEM. Schretter *et al.* extended 4D-STEM to polycrystalline materials.[9] Drouillas *et al.* compared the 4D-STEM approach to N-PED for strain analysis in semiconductor thin films.[10] The application of direct electron detectors with 4D-STEM has facilitated *in situ* measurements of strain during gas–solid interaction.[11] To minimize the calibration complexities and possible instrumental artefacts, it is vital to record the data from the undistorted part of the sample under identical experimental conditions within the same measurement session. This undistorted part is called the reference area, even though the identification of undistorted regions within an epitaxial layer grown is not always possible. On the other hand, using a single-crystal substrate as a reference can serve to eliminate problems arising from both deficiencies of calibration and instrumental distortions. Thus, in heterostructures, the differences between the lattice parameters of the substrate and the layer may help to deduce the local distortions in the layer as compared to the parameters of a free-standing undistorted layer of the same crystal structure. The situation is especially challenging if the heterostructure manifests different crystal structures in the layer compared with those in the substrate. The present paper illustrates the utility of such an approach, discussing both the necessary conditions for its applicability and the limitations of the results using differently treated and differently measured cubic γ-Ga_2O_3 layers on a monoclinic β-Ga_2O_3 substrate.

Indeed, to prove the concept, we use the recently discovered Ga_2O_3 polymorph heterostructures.[12–15] Notably, Ga_2O_3 is an interesting material, with promising applications in semiconductor technology. There are five polymorphs (rhombohedral (α), monoclinic (β), defective spinel-type cubic (γ), orthorhombic (κ), and bixbyite-like cubic (δ) phases[16–19]) of Ga_2O_3 known in the literature. The thermodynamically stable monoclinic β ($C2/m$) is available in the form of wafers. The meta-

[a]*Thin Film Physics Laboratory, Institute of Technical Physics and Materials Science, HUN-REN Centre for Energy Research, Konkoly Thege M. út 29-33, H-1121 Budapest, Hungary. E-mail: labar.janos@ek.hun-ren.hu*
[b]*University of Oslo, Department of Physics, Centre for Materials Science and Nanotechnology, PO Box 1048 Blindern, N-0316 Oslo, Norway*

This journal is © The Royal Society of Chemistry 2026

Open Access Article. Published on 02 January 2026. Downloaded on 3/3/2026 10:50:38 PM.
This article is licensed under a Creative Commons Attribution-NonCommercial 3.0 Unported Licence.

stable κ- and α-phases have been demonstrated in the form of thin films grown in certain temperature ranges. Recently, the less known cubic γ-Ga_2O_3 has become available in the form of thin layers, and the stability of this phase and its crystallographic compatibility with the stable β have attracted increasing attention from the scientific community. Therefore, measuring the strain in such layers can provide valuable information for further development of polymorph heterostructure concepts.[12–15]

We present here the common sublattice method (CSM) to extend strain measurements in epitaxial layers from the simple case of a cubic layer on a cubic substrate to the general case of a substrate with one crystal structure and a layer on it from another crystal structure. In our method, we calibrate the system by measuring an unstrained reference in the substrate, and the strain in the layer is given relative to the unstrained lattice of the layer based on an interrelation of the two structures. We demonstrate the benefits of the new method over the GPA method. We show that the new method is insensitive to either the variations of local thickness of the sample or minor variations of bending of the lamella or experimental parameters like camera length and convergence angle. Its precision is ~0.5% in strain values. Our measurements reveal anisotropic lateral strain resulting from the anisotropic lateral mismatch between the cubic γ-Ga_2O_3 layer and the monoclinic β-Ga_2O_3 substrate. We explain the variation of spatial relaxation of strain in differently treated samples by the presence of implanted Ni ions on the one hand and by differences in the tendency of back-transformation of the cubic phase into the monoclinic phase over the layer volume in differently heat-treated samples.

Results

Principles of the common sublattice method

The common sublattice method (CSM) is based on the measurement of electron diffraction patterns from thin lamellae using a transmission electron microscope (TEM) operated in microprobe scanning mode (μP-STEM). It is based on the output of a four-dimensional (4D) electron diffraction (ED) dataset processed by the 4D-ED method.[1] A two-dimensional (2D) electron diffraction spot pattern is recorded at each position while a nearly parallel electron nanobeam is scanned over a rectangular region line-by-line. While the 4D-ED method can only evaluate samples where both the reference and the measured layer have the same crystal structure (belong to the same crystallographic phase), in our new common sublattice method, the reference area is taken from one crystal structure, and the measured layer belongs to another (but closely related) crystal structure. We can easily follow the spatial distribution of the distortion of a preselected measured reciprocal lattice (diffraction pattern), and changes in this distortion clearly indicate the location of the transition from the reciprocal lattice of one structure to the reciprocal lattice of another structure.

The common sublattice is defined in reciprocal space. Let δ_1 and δ_2 be two predefined small numbers, while $\underline{\mathbf{a}}_1^*$ and $\underline{\mathbf{b}}_1^*$ are the base vectors of lattice$_1$ and $\underline{\mathbf{a}}_2^*$ and $\underline{\mathbf{b}}_2^*$ are the base vectors of lattice$_2$. If there exists a pair of reciprocal vectors $\underline{\mathbf{a}}^*$ and $\underline{\mathbf{b}}^*$ such that all the reciprocal vectors ($\underline{\mathbf{g}}_1$) of lattice$_1$ in the 2D observed reciprocal space plane (*i.e.* the diffraction pattern measured from the given zone axis orientation) are close to $n_1\cdot\underline{\mathbf{a}}^* + m_1\cdot\underline{\mathbf{b}}^*$ (*i.e.* $|n_1\cdot\underline{\mathbf{a}}^* + m_1\cdot\underline{\mathbf{b}}^* - \underline{\mathbf{g}}_1|<\delta_1$) and $n_2\cdot\underline{\mathbf{a}}^* + m_2\cdot\underline{\mathbf{b}}^*$ is close to all the reciprocal vectors ($\underline{\mathbf{g}}_2$) of lattice$_2$ (*i.e.* $|n_2\cdot\underline{\mathbf{a}}^* + m_2\cdot\underline{\mathbf{b}}^* - \underline{\mathbf{g}}_2|<\delta_2$), then linear combinations of $\underline{\mathbf{a}}^*$ and $\underline{\mathbf{b}}^*$ with integer multipliers define the common sublattice. Small deviations (δ_1 and δ_2) are treated by separate lattice matching to each pattern, irrespective of the fact that the small deviation was caused by changes in the lengths of the base vectors, the angle between them, or both. The size of the small deviations (δ_1 and δ_2) can be set at the start of operation up to the point where the spots to identify remain clearly distinguishable from other spots (see graphical abstract).

With the above conceptual framework, we can follow how the lengths of the measured surface-normal vectors ($|\underline{\mathbf{g}}_{N1}|$ and $|\underline{\mathbf{g}}_{N2}|$) and lateral vectors ($|\underline{\mathbf{g}}_{L1}|$ and $|\underline{\mathbf{g}}_{L2}|$) change in the measured patterns without the need to predefine which measured patterns belong to which phase. ($\underline{\mathbf{g}}_L$ is normal to $\underline{\mathbf{g}}_N$ in both lattices.)

In the lattice fitting procedure, we only use the measured points close to the expected positions of the common sublattice. In this way, we can use different subsets of lattice points for fitting in the different patterns. Similarly, we disregard "alien" spots.

The necessity and efficiency of the lattice-fitting approach are demonstrated during the discussion of results. The d-values are always measured from the fitted lattice.

Relative lattice distortion (strain) is determined from the d-values in the layer (d_l) and the reference area (d_{ref}).

$$\varepsilon = \frac{d_l - d_{ref}}{d_{ref}} = \frac{g_{ref} - g_l}{g_l}$$

where $g = 1/d$ in accordance with convention in electron diffraction. In contrast to the 4D-ED approach, GPA calculates

$$\varepsilon_{xx} = \frac{\partial u_x}{\partial_x} \quad \text{and} \quad \varepsilon_{yy} = \frac{\partial u_y}{\partial_y},$$

where u is the displacement vector.

When the layer is epitaxial to the substrate (as in our case), there is a strong correlation between the two respective lattices even though the lattice parameters are slightly different. In such cases, a common sublattice can be defined. When we slightly distort this common sublattice to the different diffraction patterns, we do not need to use the same diffraction spots in each pattern. When the sample is slightly tilted (bent), a few diffraction spots may be missing from the measured pattern. Since different parts of the TEM lamella may bend differently, different diffraction spots may be missing from patterns recorded in different parts of the lamella. However, the remaining (visible) spots facilitate fitting the entire lattice. In

Open Access Article. Published on 02 January 2026. Downloaded on 3/3/2026 10:50:38 PM.
This article is licensed under a Creative Commons Attribution-NonCommercial 3.0 Unported Licence.

this way, we can start with different subsets of diffraction spots in different patterns to arrive at the same entire lattice (of a structure). This procedure ensures that we can measure any point of the reciprocal lattice with equal reliability, irrespective of whether the corresponding diffraction spot is visible in the examined diffraction pattern.

The 2D distribution of deviations of the measured values from the values recorded in the reference area can be mapped over the area examined in the TEM lamella. Upon assuming that the measurement is good, these values statistically fluctuate around zero at the pixels of the reference area, and (in case of an ideally steep transition between the phases) there is a step-like jump when the map crosses the border between the substrate and the layer. In the case of undistorted layers (*i.e.*, the two structures hypothetically glued together without interaction), the size of the jump should be equal to the difference between the relevant lattice parameters between the substrate and the layer. Based on the known (and imaged) position of the substrate and of the layer in the lamella, we can subtract the jump caused by the nominal difference between these lattice parameter values, leaving a map of variations that fluctuate (with the random errors) around the values expected for an undistorted lattice at each pixel. When these deviations exceed the size of random fluctuations, they represent the local distortion of the lattice (strain) in the pre-selected direction.

Statistical reliability is improved if values from pixels at a given depth from the surface are averaged to produce a one-dimensional (1D) depth distribution that can be compared to the depth profiles of any other measured properties.

Measured deviations from reference *d*-values

In addition to our 2D maps and 1D depth distributions of changes in *d*-values, we also measure the angle between the base vectors and present their variation as a function of depth from the sample surface. In many cases (including the one treated here), the latter one serves as a sensitive indicator of the depth at which the structure changes from one crystallographic phase to the other. In the examples of gallium oxide, it sensitively shows the location of change from the β to the γ phase. We use this fact to position the model calculations relative to the measured values more accurately (see Fig. 1). Although the measured angular values may carry a systematic error due to the slight elliptical distortion of the recorded diffraction patterns (caused by the lenses of TEM), this systematic error is identical for all diffraction patterns from a given measurement, so the variation reliably shows the interface between the β and γ phases.

Fig. 1 shows the depth distribution of angles between the base vectors as a function of the position from the surface. The distance is measured along the surface normal, so positions inside the sample are described by negative numbers. The first three (Fig. 1a–c) are from lamellae cut in the [110] orientation of the layer (*i.e.*, the electron beam is incident along the [110] direction) with the surface normal pointing to (020) in the β phase (substrate) and to (440) in the γ phase (layer). We call this the normal direction. As expected, the position of the interface can be seen from the jump in the angular value for the samples as-implanted and heat treated at 300 C and at 700 C. Fig. 1d presents the angle between base vectors in a lamella cut from an orthogonal direction, the [001] orientation of the γ layer. The surface normal also points to (020) in the β phase (substrate) and to (440) in the γ phase (layer). The direction orthogonal to both the normal direction and the beam direction is called the lateral direction, given by (20−4) in β and (440) in γ.

When the Miller indices of the lateral and normal *g*-vectors (diffraction spots) are identified both in the undistorted substrate and in the undistorted layer, we can calculate relative differences between them. We call this presentation of the literature data the "Model".

We summarize the concrete literature data (based on ICSD database entries ICSD 236276 and ICSD 290282) relevant to gallium oxide phases used in the model in Tables 1 and 2, while one can see the variation of the *d*-values in the normal and lateral directions as a function of depth in Fig. 2. The overlaid variations in the Model *d*-values show how the *d*-values would change if the two phases were glued together with an abrupt interface without any strain. Note that the orientations are orthogonal in Fig. 2A and D.

One can see that the two lateral directions (from the two orthogonally cut lamellae) behave differently. The lateral misfit in the $[110]^{\gamma}$ lamella is 4.22%, while in the $[001]^{\gamma}$ lamella it is only 0.37%. Comparing Fig. 2A and D, we can see that indeed we observe large and small lateral jumps in the respective lamellae, as expected.

Strain

By removing the contribution of the model from the measured changes in *d*-values, we obtain the relevant strain components in the layer as if they were related to a reference in an undistorted region of the layer material.

Fig. 3 presents the depth variation of these strain values for the three, differently treated $[110]^{\gamma}$-oriented samples. We can identify 3 regions in both Fig. 3A (normal strain) and Fig. 3B (lateral strain): substrate region, interface region and far-from-interface region (extending to the sample surface). Since the deepest part of the substrate region was used as the reference, the strain value is expected to be close to zero there, irrespective of heat treatment. When the three measurement sets are considered together, the scatter of measured points (irrespective of colour) in the region between −460 nm and −328 nm provides the first estimate of precision.

Effect of experimental parameters

Two experimental parameters, namely, camera length and convergence angle, can influence the precision and accuracy of measuring the positions of diffraction spots, so examination of their effect is important. If the camera length is increased, the distance between any two diffraction spots increases. However, the number of diffraction spots that are available for lattice fitting decreases. When the convergence angle is

 This journal is © The Royal Society of Chemistry 2026

Open Access Article. Published on 02 January 2026. Downloaded on 3/3/2026 10:50:38 PM.
This article is licensed under a Creative Commons Attribution-NonCommercial 3.0 Unported Licence.

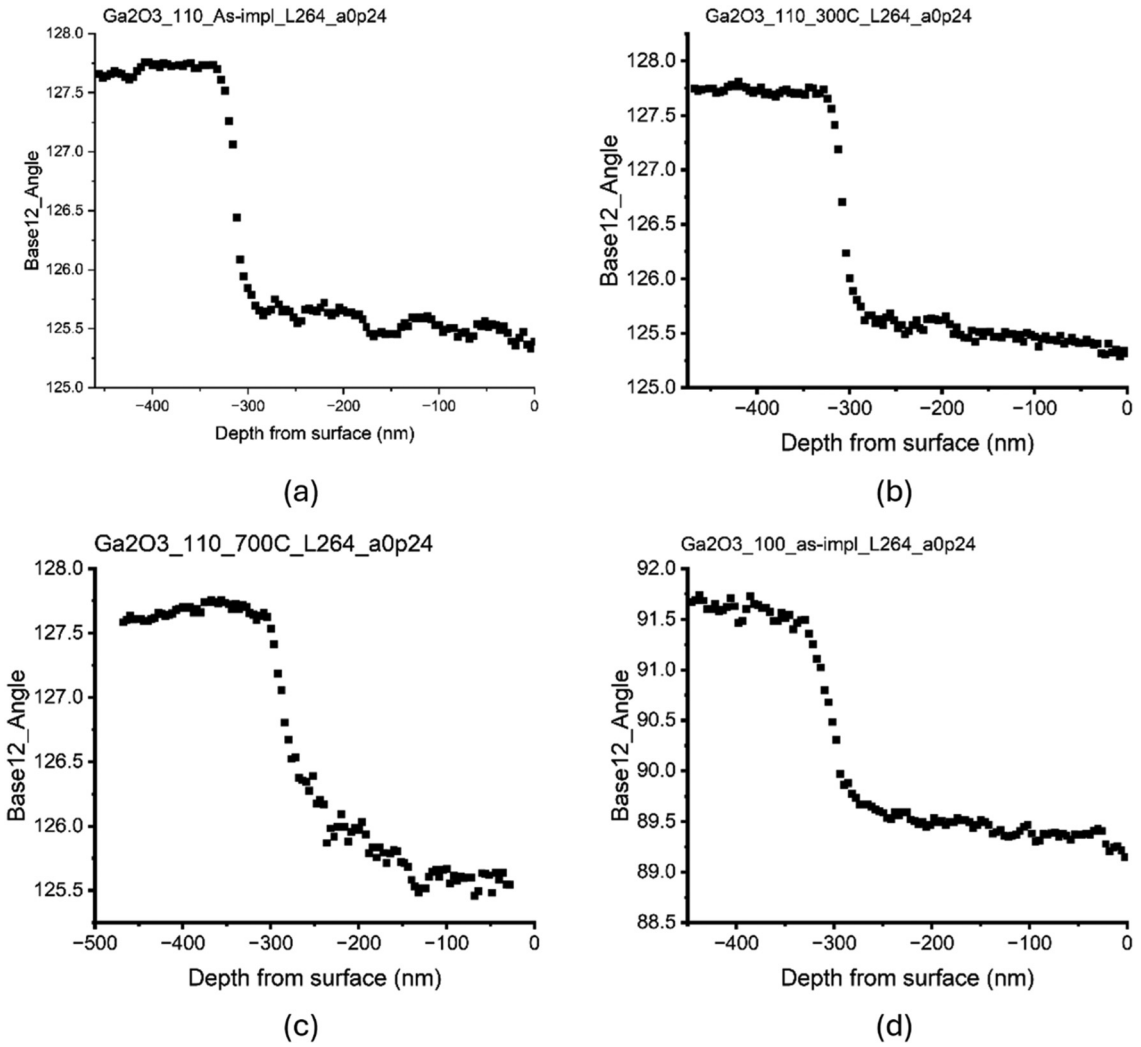

Fig. 1 Depth distribution of angles between base vectors, measured from the fitted lattices (α = 0.24 mrad and L = 264 mm). (a) As-implanted $[110]^{\gamma}$; (b) 300 C $[110]^{\gamma}$; (c) 700 C $[110]^{\gamma}$; (d) as-implanted $[001]^{\gamma}$. The steep decrease in angle values indicates the position of the interface. Note that the orientations are orthogonal in (a) and (d).

Table 1 Details of the reciprocal lattice for samples with the [110] zone of the γ-phase from literature data [ICSD 236276 and ICSD 290282]

	Index in β (SG12)	d in β (SG12) (Å)	Index in γ (SG227)	d in γ (SG227) (Å)	$\Delta d/d$ (%)
Base-1	(310)	2.4084	(444)	1.189	
Base-2	(200)	5.9276	(400)	2.0594	
Base12-angle	127.5°		125.3°		
Zone	[001]		[110]		
Normal	(020)	1.5188	(440)	1.4562	−4.12
Lateral	(600)	1.9759	(400)	2.0594	4.22

Table 2 Details of the reciprocal lattice for samples with the [001] zone of the γ-phase from literature data [ICSD 236276 and ICSD 290282]

	Index in β (SG12)	d in β (SG12) (Å)	Index in γ (SG227)	d in γ (SG227) (Å)	$\Delta d/d$ (%)
Base-1	(1 − 1 − 2)	2.0983	(400)	2.0594	
Base-2	(11 − 2)	2.0983	(040)	2.0594	
Base12-angle	92.2°		90°		
Zone	[201]		[001]		
Normal	(020)	1.5188	(440)	1.4562	−4.12
Lateral	(20 − 4)	1.4509	(440)	1.4562	0.37

increased, the size of the probe decreases, and spatial resolution improves. However, the diffraction spot extends to a small disk with an inner structure (in thicker samples), so the reliability of localization can be reduced.

To study the effect of these parameters, we repeated the same measurements (in new locations) with three experimental parameter sets (1: camera length, L = 327 mm, and convergence angle, α = 0.24 mrad; 2: L = 264 mm and α = 0.24 mrad; and 3: L = 264 mm and α = 0.34 mrad). The three sets are plotted in different colours in Fig. 4 (Fig. 4A for the normal direction and Fig. 4B for the lateral direction). If we treat the three sets together (disregarding colour), the scatter of points in Fig. 4 provides an estimate of precision. Linear fits to the consolidated dataset (containing all 3 measurement

Open Access Article. Published on 02 January 2026. Downloaded on 3/3/2026 10:50:38 PM.
This article is licensed under a Creative Commons Attribution-NonCommercial 3.0 Unported Licence.

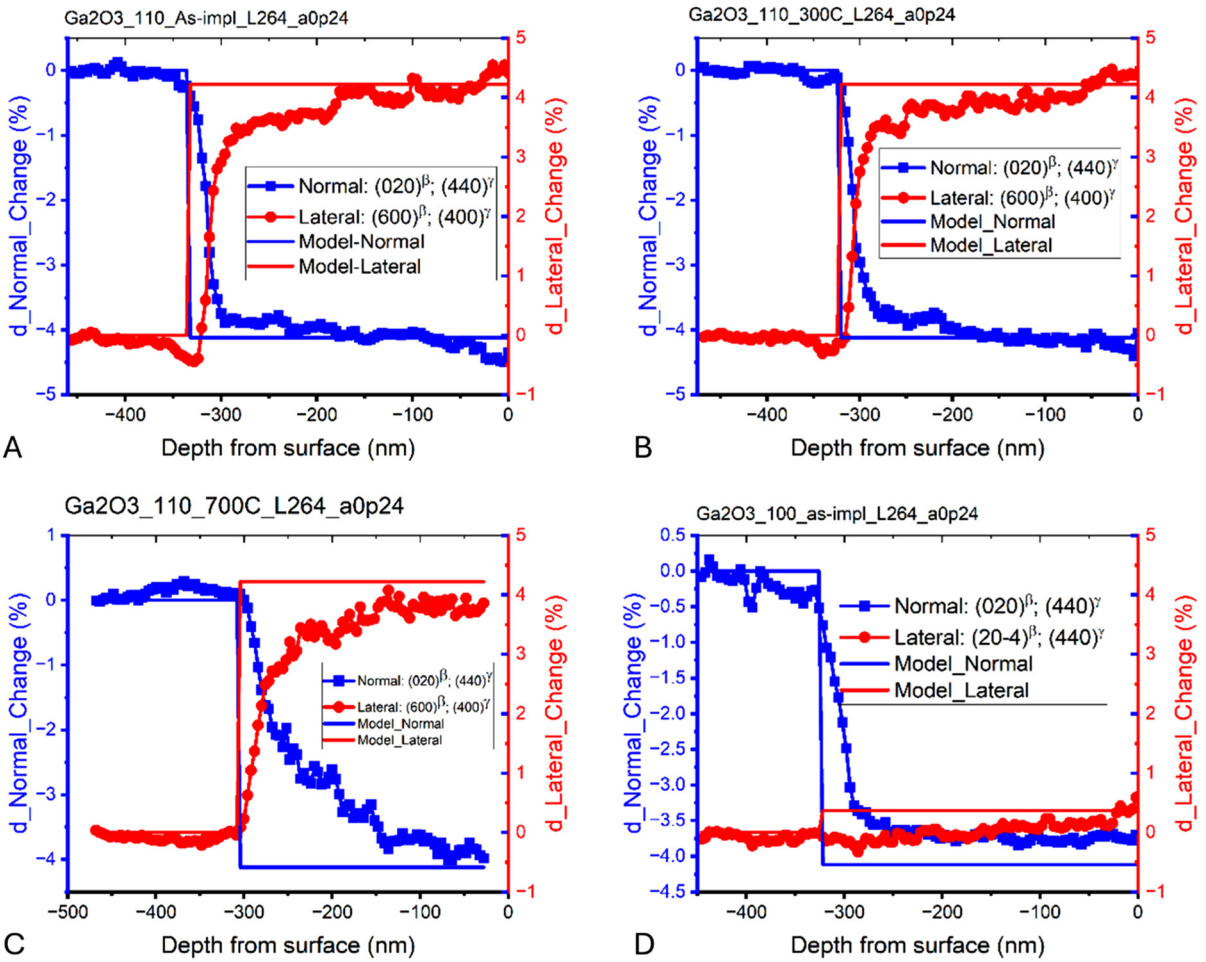

Fig. 2 Depth distribution of measured changes in *d*-values together with changes in *d*-values of the Model. Blue = normal component. Red = lateral component (α = 0.24 mrad and L = 264 mm). (A) As-implanted $[110]^{\gamma}$; (B) 300 C $[110]^{\gamma}$; (C) 700 C $[110]^{\gamma}$; (D) as-implanted $[001]^{\gamma}$. Deviations of the measured values (symbols) from the Model (lines) indicate the presence of strain (see Fig. 3 and 4). Note that the orientations are orthogonal in (A) and (D).

sets) are shown to provide trend lines for the individual regions. If we disregard the observed trends in either the substrate region or in the far-from-interface region and interpret any variation of data as if they were statistical scattering of data, we obtain a conservative overestimation of the standard deviation (precision).

Fig. 4 supports our claim that the precision of 0.5% in strain values is a conservative estimate. Tables 3 and 4 summarize the statistical evaluation of the consolidated data in the substrate region and in the far-from-interface region. They also confirm that reproducibility is better than the claimed 0.5% in strain values (the standard deviation (σ) of the data for normal strain in both regions is 0.18% and 0.23%, respectively, and for lateral strain, it is 0.19% and 0.07%, respectively).

Discussion

In Fig. 3 (as-implanted sample in the $[110]^{\gamma}$ orientation), the black squares show the averaged in-plane (lateral) and out-of-plane (normal) strain components across the layer including the substrate β-Ga_2O_3 and the transformed γ-Ga_2O_3 layer. Three main parts of the strain curves can be differentiated and are discussed in detail: (1) the β → γ transformation front, (2) *ca.* 35 nm wide range after the transformation front (interface region), where the slope of the strain curves is high, and (3) the range up to the top of the layer (far-from-interface region), where the slope of the strain curves is low. The implantation depth, where the strain curve shows a sharp jump/step, is found to be 320 nm (±10). At the transformation front, the top of the β substrate probably exhibits slight compressive strain (deduced from the trend line in Fig. 4), while γ shows 3.75% out-of-plane tensile strain and −4% in-plane compressive strain. After the β/γ transformation front, within *ca.* 35 nm, most of the strain is relaxed and reaches +0.4% in the normal direction (tensile strain), while it is −1% in the lateral direction (compression strain), and further upward in the layer, they start to approach zero value, which is valid for a fully relaxed structure. Energy-dispersive X-ray spectrometry (EDS) depth profiles (Fig. 5) showed that Ni accumulates in the lower

 This journal is © The Royal Society of Chemistry 2026

Open Access Article. Published on 02 January 2026. Downloaded on 3/3/2026 10:50:38 PM.
This article is licensed under a Creative Commons Attribution-NonCommercial 3.0 Unported Licence.

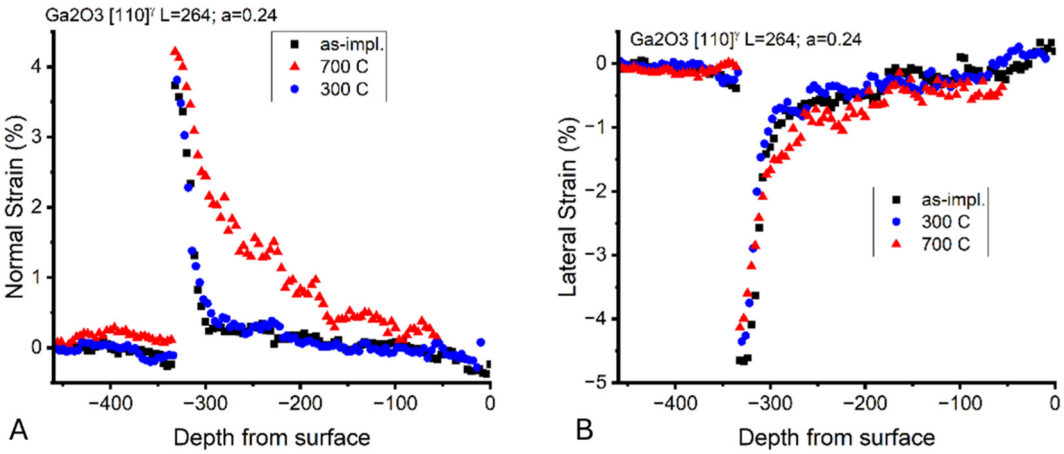

Fig. 3 Variation of depth distribution of strain in samples with different heat treatments. (α = 0.24 mrad and L = 264 mm. Beam direction = sample orientation $[110]^{\gamma}$). Black squares = as-implanted. Blue circles = heat treated at 300 C. Red triangles = heat treated at 700 C. (A) Normal strain (in direction of $(020)^{\beta}||(440)^{\gamma}$). (B) Lateral strain (in the direction of $(600)^{\beta}||(400)^{\gamma}$). Three spatial sections are identified: substrate region (from −460 nm to −328 nm), interface region (from −324 nm to −292 nm) and far-from-interface region (close to surface) (from −288 nm to 0 nm). Strain is close to zero in the substrate region, as expected. A steep change is observed in the interface region. Strain curves for the as-implanted and 300 C samples coincide within the statistical scatter, while the 700 C sample shows a much slower variation of strain in the far-from-interface region.

part (~150–200 nm depth) of the layer (at maximum ~<1 at%; Fig. 5), which could be coherent with the strain curve. These imply that the measured strain at the transformation front (+3.75% and −4%) originates from the lattice mismatch between β and γ (that is mostly relaxed after *ca.* 35 nm), while the later low slope of the curve can be attributed to defects induced by the implant atom (Ni).

Detailed EDS mapping did not provide evidence of Ni segregation in any of the measured samples. Compositional quantification of Ni in the layer is very limited since the Ni amount is around the detection limit of the EDS method. That is why EDS elemental maps cannot be provided, only the depth profiles, which are presented in Fig. 5. However, an enhanced concentration due to segregation would be seen in the EDS, and we have not observed such an enhancement.

Fig. 4 (as-implanted sample in the orthogonally cut $[100]^{\gamma}$ orientation) shows the averaged in-plane (lateral) and out-of-plane (normal) strain components as a function of depth. Since it is measured with three different experimental parameters at slightly different locations on the sample, they also provide an estimate of reproducibility and demonstrate the lack of sensitivity to experimental parameters (camera length and convergence angle). One can see that the measured normal strain component is identical to the value measured in the orthogonally cut lamella (as it should), but the lateral strain is negligible in this direction. Fig. 2D shows that the striking differences in the variation of the measured lengths of laterally pointing diffraction vectors coincide with the expected small jump due to the change in structure as we cross the β/γ interface. The theoretical mismatch is conspicuously different in the two orthogonal lateral directions. This fact explains the size of the normal strain that tries to minimize volume change (~−4% in one lateral direction, ~0% in the other lateral direction and ~+4% in the normal direction, resulting in close to zero volume change, as expected for elastic deformation).

Annealing of the sample at 300 °C only caused slight changes in the strain curve (Fig. 3). The most striking difference compared to the non-annealed sample is the depth of the γ Ga_2O_3 layer, which is *ca.* 10 nm less, *i.e.*, the thickness of the γ layer has decreased to ~310 nm. This indicates that the (back)transformation from γ → β has started at the interface front. Meanwhile, the compressive strain measured at the top of the β substrate in the as-implanted sample has disappeared/relaxed. Parallel to this, the in-plane compressive and out-of-plane tensile strains seem to slightly increase, but the change remains within the error of the measurement. After the transformation front with *ca.* 35 nm, the slope of the curve is very similar to the strain curves measured in the as-implanted sample. Energy-dispersive X-ray spectroscopy (EDS) depth distributions showed the same Ni distribution in all three samples (Fig. 5).

Annealing of the sample at 700 °C caused more significant changes. At this annealing temperature, γ transforms back to β not only at the interface but also inside the γ layer, as we documented this in individual ED patterns. Therefore, the slope of the strain curve beyond the transformation front (Fig. 3) shows more out-of-plane tensile and in-plane compressive strains with a slower decrease toward the surface caused by the coexistence of both polymorphs. This also implies an increasing relative amount of β closer to the interface. The maximum measured strain values of the layer at the interface are +4% out-of-plane tensile strain and −4% in-plane compressive strain. As a continuation of the tendency/trend, the transformation front γ → β shifts further into the layer that results in a decreased thickness (304 nm + −10 nm) of the layer containing the γ phase.

Open Access Article. Published on 02 January 2026. Downloaded on 3/3/2026 10:50:38 PM.
This article is licensed under a Creative Commons Attribution-NonCommercial 3.0 Unported Licence.

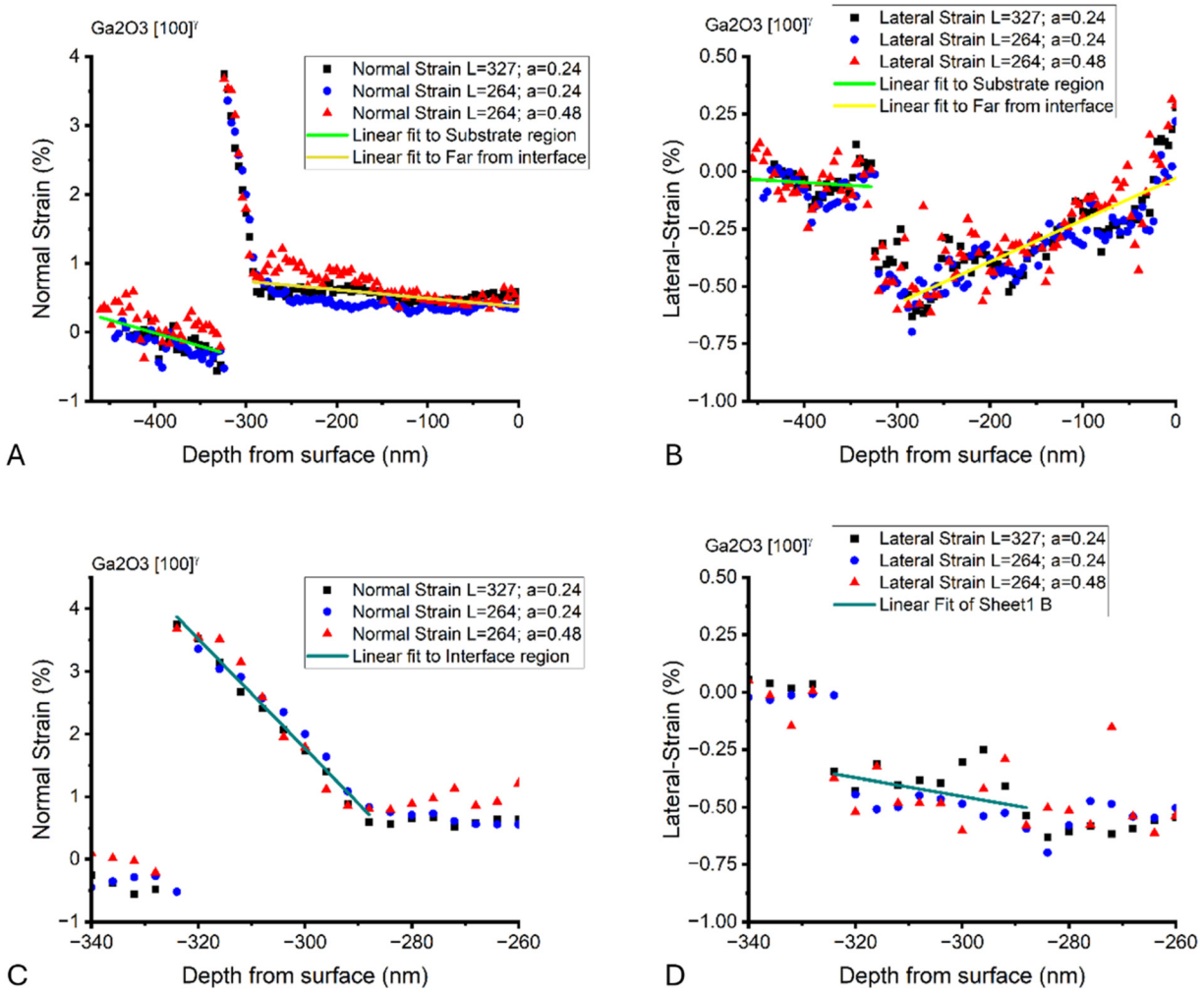

Fig. 4 Variation of depth distribution of strain measured under different experimental conditions to test reproducibility. Orientation: $[100]^{\gamma}$. Black squares: camera length, L = 327 mm; convergence angle, α = 0.24 mrad. Blue circles: L = 264 mm, α = 0.24 mrad. Red triangles: L = 264 mm, α = 0.48 mrad. (A) and (C) Normal strain (in the direction of $(020)^{\beta}||(440)^{\gamma}$). (B) and (D) Lateral strain (in the direction of $(20{-}4)^{\beta}||(440)^{\gamma}$). Three spatial sections are identified: substrate region (from −460 nm to −328 nm), interface region (from −324 nm to −292 nm) and far-from-interface region (up to the surface) (from −288 nm to 0 nm). A slight (~10 nm) shift of the curves was applied to bring the interface into coincidence in all three measurements facilitating comparison of trends between the samples. Linear fits to the consolidated dataset (containing all 3 measurement sets) are shown to provide trend lines in the individual regions. Scatter of points (when colour is disregarded) gives an estimate of precision, while quantified results of statistical evaluations are summarized in Tables 3 and 4. (C) and (D) Magnified views of the interface region. The three datasets produce the same trend in the interface region, too. The scatter of data is also low in this region.

Experimental

Preparation of the samples

TEM lamellae were prepared with a Thermo Fisher Scientific Scios 2 Dual Beam microscope (Eindhoven, The Netherlands) with an EasyLift™ nanomanipulator. First, a Pt layer was deposited onto the lamella to protect the layer during ion milling. Thinning of the lamellae (after digging trenches on both sides) was carried out in four steps using Ga ions: (1) down to a lamella thickness of 400 nm – at 2.5° on both sides with 16 kV per 50 pA; (2) down to a lamella thickness of 150 nm – at 2.5° on both sides with 8 kV per 25 pA; (3) for polishing at 5° on both sides with 5 kV per 48 pA; and (4) for the final polishing at 7° on both sides with 2 kV per 27 pA. The detailed preparation protocol was developed just for these types of samples to reduce any artefact below the observable level. Additionally, the beta substrate, which was prepared at the same time, shows no emerged/increased dislocation density, amorphization, or any other unusual damage. To test this effect, final polishing of the FIB sample was also performed with Ar ions for comparison. No changes were observed. This is why the effect of Ga-ion incorporation was not considered in the error analysis.

Instrumentation

Experimental data for the 4D-ED dataset were collected using a Titan Themis G2 200 STEM (Thermo Fisher Scientific, Waltham, MA, USA) equipped with an X-FEG gun and a 4k ×

 This journal is © The Royal Society of Chemistry 2026

Open Access Article. Published on 02 January 2026. Downloaded on 3/3/2026 10:50:38 PM.
This article is licensed under a Creative Commons Attribution-NonCommercial 3.0 Unported Licence.

Table 3 Normal strain (in the direction of $(020)^{\beta}||(440)^{\gamma}$). Orientation: $[100]^{\gamma}$. The result of statistical evaluation of the consolidated data points from 3 sets of measurements (disregarding colour in Fig. 4a). The observed trends in both the substrate region and in the far-from-interface region were disregarded, and variations in data were interpreted as statistical scatter to obtain a conservative overestimation of standard deviation (precision)

Range [nm]	Minimum	Maximum	Median	Mean	Standard deviation
0 to −292 far from the interface	0.27	1.21	0.51	0.55	0.18
−328 to −460 substrate region	−0.56	0.59	−0.08	−0.06	0.23

Table 4 Lateral strain (in the direction of $(20\text{-}4)^{\beta}||(440)^{\gamma}$). Orientation: $[100]^{\gamma}$. The result of statistical evaluation of the consolidated data points from 3 sets of measurements (disregarding colour in Fig. 4b). The observed trends in both the substrate region and in the far-from-interface region were disregarded, and variations in data were interpreted as statistical scatter to obtain a conservative overestimation of standard deviation (precision)

Range [nm]	Minimum	Maximum	Median	Mean	Standard deviation
0 to −292 far from the interface	−0.7	0.31	−0.31	−0.29	0.19
−328 to −460 substrate region	−0.24	0.12	−0.05	−0.05	0.07

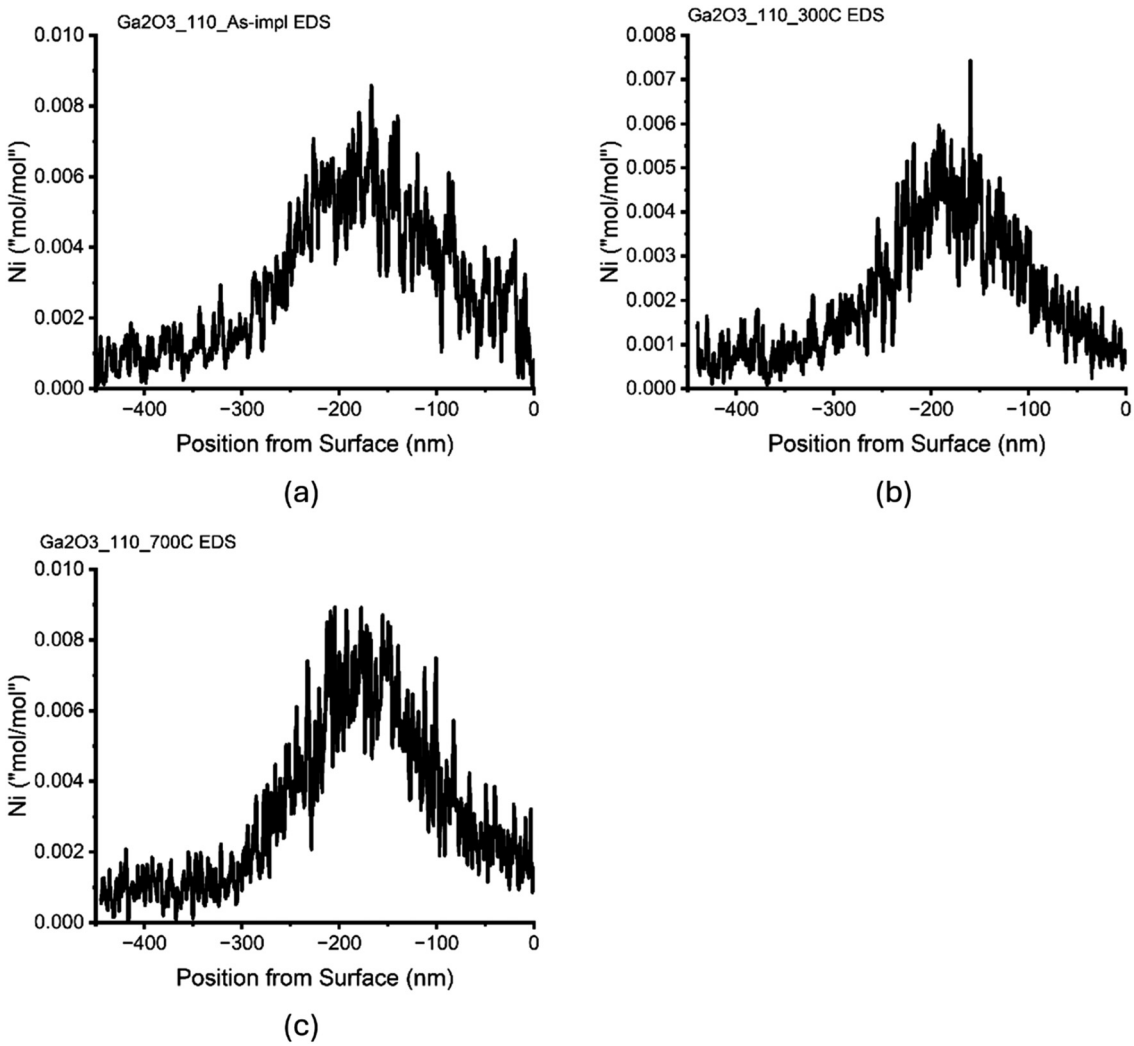

Fig. 5 Depth distribution of Ni measured by energy-dispersive X-ray spectrometry (EDS): (a) as-implanted; (b) 300 C; (c) 700 C.

4k CETA16 CMOS camera (Thermo Fisher Scientific, Waltham, MA, USA). The STEM was in microprobe STEM mode of operation during data collection that was controlled using TIA software (FEI, Eindhoven, The Netherlands). STEM *Z*-contrast images were recorded with a high-angle annular dark-field (HAADF) detector (E.A. Fischione Instruments, Inc.,

Open Access Article. Published on 02 January 2026. Downloaded on 3/3/2026 10:50:38 PM.
This article is licensed under a Creative Commons Attribution-NonCommercial 3.0 Unported Licence.

Pennsylvania, PA, USA) controlled using Velox software (version 3.3, FEI, Eindhoven, The Netherlands). TEM characterization and recording of TEM images prior to the 4D-ED experiment were performed with the same CETA camera, which was later used to record the diffraction patterns. We used the 4D-ED program[1] to measure spatial changes in *d*-values. We prepared the graphs for the manuscript using the Origin 2024 program (© 1991–2024 OriginLab Corporation).

Experimental conditions for the measurements

The illuminating electron beam is almost parallel (convergence angle, α = 0.24 mrad) in this mode of operation, providing spots in the diffraction pattern in contrast to the extended discs observed in conventional STEM mode, which uses a larger convergence, similar to convergent beam electron diffraction (CBED). The selection of these parameters is a trade-off between spatial resolution (which is full width at half maximum (FWHM) = 1.97 nm for α = 0.5 mrad and 3.65 nm for α = 0.24 mrad in our case, as shown in Fig. 6) and size of diffraction spots (which are comparable to that observed in selected area electron diffraction (SAED)). When the convergence angle is increased to 0.48 mrad, the diffraction spots expand into small disks with occasional inner structure, depending on the structure and thickness of the sample. Measurements at this increased convergence could pose a challenge to our procedures for measuring distances of spots accurately. However, the results show that the procedure works well even for this convergence. 100 ms dwell time per pixel was applied to collect the diffraction patterns. The STEM operated at 200 keV. Two distinct camera lengths were applied to validate that the results do not depend on this experimental parameter. The camera lengths (L = 264 mm and L = 327 mm) were calibrated on diffraction patterns recorded at the reference areas. We used spot size 9 to ensure strong enough diffraction spots, helping to process without oversaturating or damaging the camera. Our complementary metal–oxide-semiconductor (CMOS) camera allowed combining the readout of several pixels at the hardware level and restricting the collection of patterns to sub-parts of the camera. Since 512 × 512 pixel diffraction patterns proved to be good enough for our processing, we used a quarter of the entire camera with sampling 2, which reads out intensity from 2 × 2 pixels as a single value, resulting in an effective camera pixel size of 28 μm. The final sample area, for the 4D-ED experiment, the field of view (FOV), was selected within an HAADF image, and the marked area was divided into a preselected number of columns (N_{column}) and rows (N_{row}). This defines the lateral spatial resolution that is called the step size for the STEM image (step size). Identical step sizes were selected in the x and y directions. By combining it with the local sample thickness (t), we could obtain the size of the voxel, the excited volume (V = step size × step size × t) that produces the measured signal. A step size = 4 nm was used in the experiments reported here. The typical sample thickness varied between 50 nm and 150 nm. The number of measured diffraction patterns is given by $N_{\mathrm{pattern}} = N_{\mathrm{colum}} \times N_{\mathrm{row}}$. N_{pattern} = 125 × 15 = 1875 was used for the measurements in the present publication.

Details of the reciprocal lattice for samples with the $[110]^{\gamma}$ zone

In this series of images, the selected sublattice is generated with Base-1 vector = $(310)^{\beta}$ and Base-2 vector = $(-200)^{\beta}$ with an angle = 127.5° between them.

This sublattice is slightly distorted by the lattice-fitting procedure, resulting in 2 × Base-1 vector ≅ $(44 - 4)^{\gamma}$, 3 × Base 2 vector ≅ $(-400)^{\gamma}$ with an angle = 125.3° between them.

Table 1 summarizes the parameters and Fig. 7a and b show the indexing of the relevant patterns in both the substrate and the layer.

The lattice of the unstrained layer is stretched in the lateral direction by 4.22% and compressed in the normal direction by −4.12%. The sizes of the two strains are similar. Assuming elastic distortion, if the lateral strain were of similar size in the two orthogonal lateral directions, it would imply a significant change in volume.

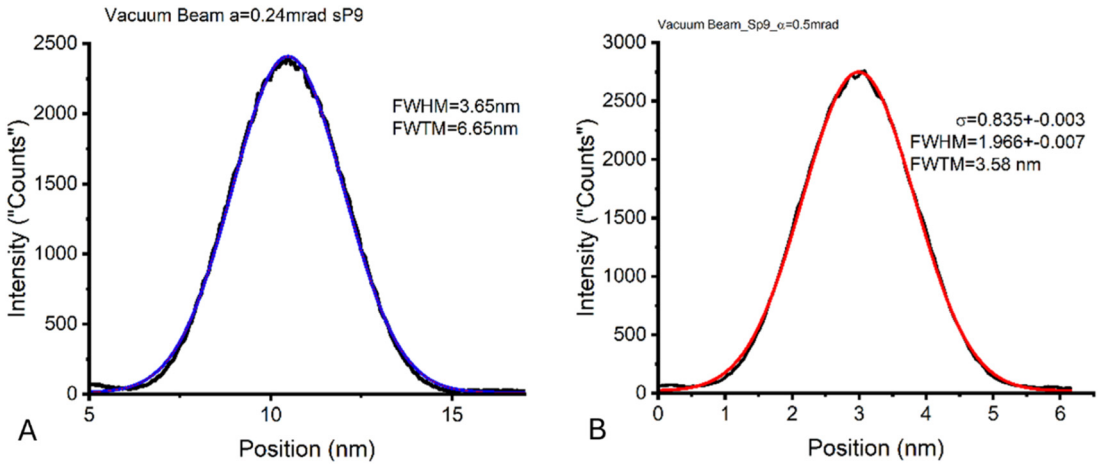

Fig. 6 Probe size from the intensity profile through the image of the beam for two values of convergence angles. FWHM = full width at half maximum. FWTM = full width at tenth of maximum. (A) Convergence angle, α = 0.24 mrad, FWHM = 3.65 nm; (B) α = 0.5 mrad, FWHM = 1.97 nm.

Open Access Article. Published on 02 January 2026. Downloaded on 3/3/2026 10:50:38 PM.
This article is licensed under a Creative Commons Attribution-NonCommercial 3.0 Unported Licence.

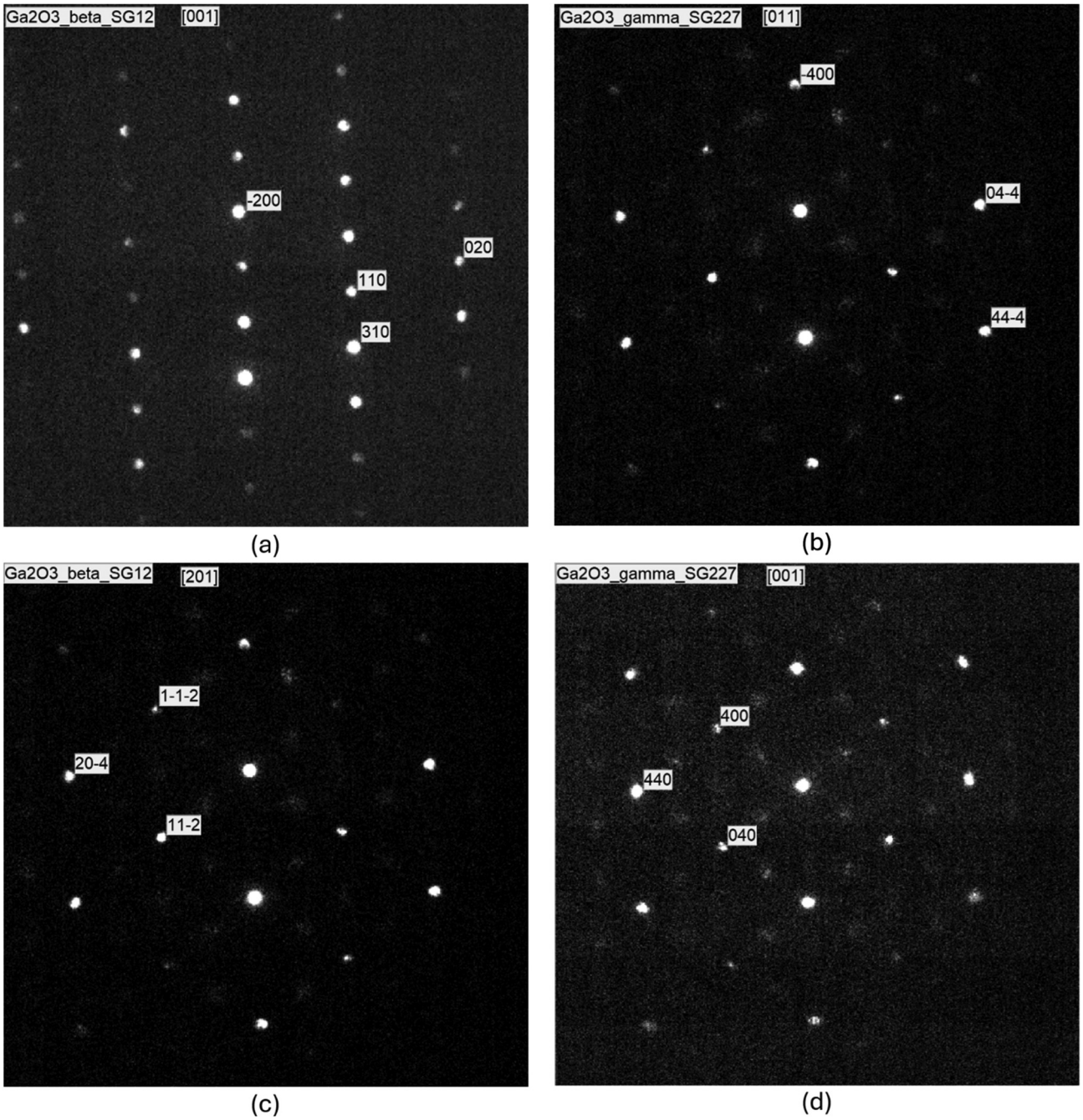

Fig. 7 Details of reciprocal lattice. (a) Indexed pattern from the substrate: samples with $[110]^{\gamma}$ zone; (b) indexed pattern from the layer: samples with $[110]^{\gamma}$ zone; (c) indexed pattern from the substrate: samples with $[001]^{\gamma}$ zone; (d) indexed pattern from the layer: samples with $[001]^{\gamma}$ zone. The sample surface points to the top of these patterns (direction of 200^{β} type reflections).

Details of the reciprocal lattice for samples with the $[001]^{\gamma}$ zone

In this series of images, the selected sublattice is generated with Base-1 vector = $(11-2)^{\beta}$ and Base-2 vector = $(-1-12)^{\beta}$ with an angle = 92.8° between them.

This sublattice is slightly distorted by the lattice-fitting procedure, resulting in 1 × Base-1 vector ≅ $(040)^{\gamma}$, 1 × Base 2 vector ≅ $(400)^{\gamma}$ with an angle = 90° between them.

Table 2 summarizes the parameters and Fig. 7c and d show the indexing of the relevant patterns in both the substrate and the layer.

The lattice of the unstrained layer is stretched in the lateral direction by 0.37% and compressed in the normal direction by −4.12%. It is seen that the two orthogonal lateral directions require different distortions of the layer to fit the substrate, while the change in normal direction is identical, as expected.

Open Access Article. Published on 02 January 2026. Downloaded on 3/3/2026 10:50:38 PM.
This article is licensed under a Creative Commons Attribution-NonCommercial 3.0 Unported Licence.

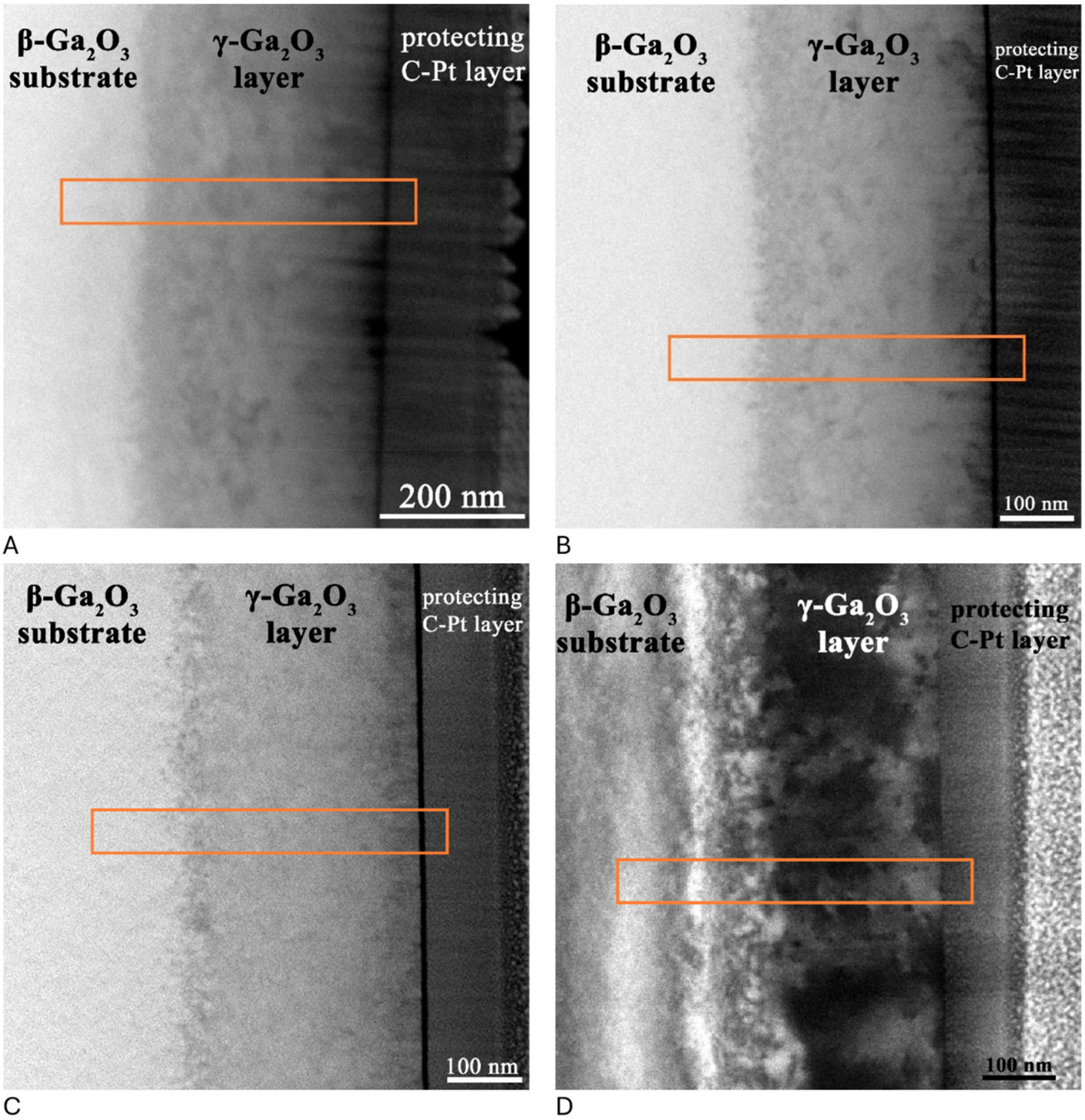

Fig. 8 Area selection for individual measurements. (A) As-implanted $[110]^{\gamma}$; (B) 300 C $[110]^{\gamma}$; (C) 700 C $[110]^{\gamma}$; (D) as-implanted $[001]^{\gamma}$. The sample surface is visible vertically on the right side of the images. A C–Pt protective layer is visible on top of the samples that was deposited during FIB milling. The rectangle indicates the area used for 4D-ED data collection. The substrate (part of which is used as a reference) is on the left side of the image. Since the STEM image was rotated 90° to bring the surface on the right side, and the diffraction does not rotate with the scan direction, the sample surface points to the top of the image in Fig. 7 which shows the indexed diffraction patterns.

With that anisotropy in lateral stretching, we do not expect a significant change in volume.

Unique parameters of the individual measurements

The first four measurements were carried out under identical conditions (L = 264 mm; convergence angle, α = 0.24 mrad; on a scanned grid of 125 × 15 points with 4 nm step-size, resulting in a 500 nm × 60 nm scanned area). The TEM lamella called TEM-1 was cut from the as-implanted sample with $[110]^{\gamma}$ orientation. TEM-2 and -3 are from the same orientation and heat treated at 300 C and 700 C, respectively. TEM-4 (as-implanted sample from $[001]^{\gamma}$ orientation) proves that there is strong anisotropy of strain in the lateral plane. TEM-5 and TEM-6 differ from the first 4 in the value of the convergence

 This journal is © The Royal Society of Chemistry 2026

Open Access Article. Published on 02 January 2026. Downloaded on 3/3/2026 10:50:38 PM.
This article is licensed under a Creative Commons Attribution-NonCommercial 3.0 Unported Licence.

angle and prove that the same strain can be measured despite the more challenging localization of disk centres due to the inner intensity distribution. TEM-7 is measured with a different camera length.

TEM-5, TEM-6 and TEM-7 contain the untreated, as-implanted layer of γ Ga_2O_3 on a β Ga_2O_3 substrate measured under different experimental parameters. All three prove the lateral non-isotropic strain. Simultaneously, they also prove that the method is robust to changes in camera length and convergence angle.

The measured area and step size were selected graphically in an HAADF image. A HAADF image of the selected area was also recorded simultaneously with the diffraction patterns. The sample surface was oriented vertically for the measurements, so any drift in the *x*-direction appears in the HAADF image as a virtual tilt of the surface. The composition of both the substrate and the layer is identical (Ga_2O_3). Since the HAADF image of a sample with homogeneous atomic composition reflects the variations in the local thickness of the TEM lamella, one can see from Fig. 8 that in all samples, the local thickness varies significantly within the area of the measurement. The results give strong proof that our method is insensitive to variations in sample thickness in contrast to the sensitivity of the HRTEM-based GPA methods.

Conclusions

The common sublattice method deduces references in the unstrained substrate (with one crystal structure) to determine the local lattice deformations in the layer (with another crystal structure). The method works if there is a common sublattice in the layer and the substrate (which is fulfilled in all epitaxial configurations), so that the deviations from it may be used to interrelate the experimentally recorded data. The new method overcomes several severe limitations of the geometrical phase analysis method, *e.g.*, having a limited field of view and the requirement to resolve the lattice image which may be constrained by camera size for large areas to examine. Furthermore, our method is insensitive to lamella thickness variations. Measurements on lamellae cut from orthogonal crystal orientations revealed non-isotropic lateral strain in Ga_2O_3 layers. The reliability was further proven by collecting data under different camera lengths, convergence angle conditions, and variable lamella thicknesses. The consistency of the results shows the usefulness of the method.

Author contributions

Equal contribution: J. L. L. and I. C.; conceptualization: J. L. L. and I. C.; methodology: J. L. L., B. P. and I. C.; software: J. L. L.; validation: J. L. L., B. P. and I. C.; investigation: J. L. L., B. P., A. A., A. K. and I. C.; data curation: J. L. L. and I. C.; writing – original draft preparation: J. L. L., A. K. and I. C.; writing – review and editing: J. L. L., B. P., A. K., A. A. and I. C.; visualization: J. L. L.; and funding acquisition: B. P., A. K. and I. C. All authors have read and agreed to the published version of the manuscript.

Conflicts of interest

There are no conflicts to declare.

Data availability

Data for this article, including csv, png and pdf files, are available at the ARP Research Data Repository at https://hdl.handle.net/21.15109/ARP/KZTIUB.

Acknowledgements

The authors are indebted to Noémi Szász for the preparation of TEM lamellae by FIB. This research was funded by the National Office for Research and Development, grant number TKP2021-NKTA-05. Transmission electron microscopy was supported by the VEKOP-2.3.3-15-2016-00002 infrastructure project funded by the State Treasury. I. Cora gratefully thanks the János Bolyai Research Scholarship of the Hungarian Academy of Sciences for their support. A. K. acknowledges M-ERA.NET Program for financial support *via* the GOFIB project (administered by the Research Council of Norway, project number 337627). Additional support for A. K. was received from the DIOGO project, funded by the Research Council of Norway in the frame of the FRIPRO Program, project number 351033. The experimental infrastructures for ion implantation were provided at the Norwegian Micro- and Nano-Fabrication Facility, NorFab, supported by the Research Council of Norway project number 295864.

References

1 J. L. Lábár, B. Pécz, A. van Waveren, G. Hallais, L. Desvignes and F. Chiodi, Strain Measurement in Single Crystals by 4D-ED, *Nanomaterials*, 2023, **13**, 1007, DOI: 10.3390/nano13061007.
2 C. Gammer, M.-I. Richard and C. Eberl, Measurement of local strain, *MRS Bull.*, 2019, **44**, 459–464, https://www.mrs.org/bulletin.
3 P. L. Galindo, S. Kret, A. M. Sanchez, J.-Y. Laval, A. Yá ez, J. Pizarro, E. Guerrero, T. Ben and S. I. Molina, The Peak Pairs algorithm for strain mapping from HRTEM images, *Ultramicroscopy*, 2007, **107**, 1186–1193, DOI: 10.1016/j.ultramic.2007.01.019.
4 J. S. Chen, Y. Liu, Y. Zhai and t. X. Fan, A new method to reliably determine elastic strain of various crystal structures from atomic resolution images, *Sci. Rep.*, 2019, **9**, 16399, DOI: 10.1038/s41598-019-52634-3.

Open Access Article. Published on 02 January 2026. Downloaded on 3/3/2026 10:50:38 PM.
This article is licensed under a Creative Commons Attribution-NonCommercial 3.0 Unported Licence.

5 C. Ophus, Four-Dimensional Scanning Transmission Electron Microscopy (4D-STEM): From Scanning Nanodiffraction to Ptychography and Beyond, *Microsc. Microanal.*, 2019, **25**, 563–582, DOI: 10.1017/S1431927619000497.
6 M. J. Hytch, E. Snoeck and R. Kilaas, Quantitative measurement of displacement and strain fields from HREM micrographs, *Ultramicroscopy*, 1998, **74**, 131–146, DOI: 10.1016/S0304-3991(98)00035-7.
7 S. Feng and Z. Xu, Strain Characterization in Two-Dimensional Crystals, *Materials*, 2021, **14**, 4460, DOI: 10.3390/ma14164460.
8 S. Wang, T. B. Eldred, J. G. Smith and W. Gao, AutoDisk: Automated diffraction processing and strain mapping in 4D-STEM, *Ultramicroscopy*, 2022, **236**, 113513, DOI: 10.1016/j.ultramic.2022.113513.
9 L. Schretter, J. Eckert and C. Gammer, Extending 4D-STEM based strain mapping to polycrystalline materials, BIO Web of Conferences, 2024, vol. 129, p. 23006. DOI: 10.1051/bioconf/202412923006.
10 E. Drouillas, J.-G. Mattei and B. Warot-Fonrose, Comparative electron diffraction analysis of strain relaxation in AlxGa1-xN materials in the microelectronics industry: 4D-STEM approach vs, TEM-based N-PED solution, *Micron*, 2025, **190**, 103785, DOI: 10.1016/j.micron.2025.103785.
11 A. Gomez-Perez, K. Wang, S. Nicolopoulos, H. Pérez-Garza and Y. Yang, In situ nanometer-resolution strain and orientation mapping for gas-solid reactions via precession-assisted four-dimensional scanning transmission electron microscopy, *Nano Today*, 2025, **64**, 102784, DOI: 10.1016/j.nantod.2025.102784.
12 A. Azarov, J. G. Fernández, J. Zhao, F. Djurabekova, H. He, R. He, Ø. Prytz, L. Vines, U. Bektas, P. Chekhonin, N. Klingner, G. Hlawacek and A. Kuznetsov, Universal radiation tolerant semiconductor, *Nat. Commun.*, 2023, **14**, 4855, DOI: 10.1038/s41467-023-40588-0.
13 T. Yoo, X. Xia, F. Ren, A. Jacobs, M. J. Tadjer, S. Pearton and H. Kim, Atomic-scale characterization of structural damage and recovery in Sn ion-implanted β-Ga_2O_3, *Appl. Phys. Lett.*, 2022, **121**, 072111, DOI: 10.1063/5.0099915.
14 H.-L. Huang, C. Chae, J. M. Johnson, A. Senckowski, S. Sharma, U. Singisetti, M. H. Wong and J. Hwang, Atomic scale defect formation and phase transformation in Si implanted *β*-Ga_2O_3, *APL Mater.*, 2023, **11**, 061113, DOI: 10.1063/5.0134467.
15 A. Azarov, A. Galeckas, I. Cora, Z. Fogarassy, V. Venkatachalapathy, E. Monakhov and A. Kuznetsov, Optical Activity and Phase Transformations in γ/β Ga2O3 Bilayers Under Annealing, *Adv. Opt. Mater.*, 2024, 2401325, DOI: 10.1002/adom.202401325.
16 H. Y. Playford, A. C. Hannon, E. R. Barney and R. Walton, I.: Structures of Uncharacterised Polymorphs of Gallium Oxide from Total Neutron Diffraction, *Chem. – Eur. J.*, 2013, **19**, 2803, DOI: 10.1002/chem.201203359.
17 I. Cora, F. Mezzadri, F. Boschi, M. Bosi, M. Caplovicova, G. Calestani, I. Dódony, B. Pécz and R. Fornari, The real structure of ε-Ga_2O_3 and its relation to κ-phase, *CrystEngComm*, 2017, **19**, 1509, DOI: 10.1039/C7CE00123A.
18 T. Kato, H. Nishinaka, K. Shimazoe, K. Kanegae and M. Yoshimoto, Demonstration of Bixbyite-Structured δ-Ga_2O_3 Thin Films Using β-Fe_2O_3 Buffer Layers by Mist Chemical Vapor Deposition, *ACS Appl. Electron. Mater.*, 2023, **5**, 1715, DOI: 10.1021/acsaelm.2c01750.
19 L. Li, W. Wei and M. Behrens, Synthesis and characterization of α-, β-, and γ-Ga_2o_3 prepared from aqueous solutions by controlled precipitation, *Solid State Sci.*, 2012, **14**, 971, DOI: 10.1016/j.solidstatesciences.2012.04.037.

 This journal is © The Royal Society of Chemistry 2026